SUPPLEMENTARY INFORMATION

doi:10.1038/nature11559

1. DEVICE DESIGN AND MEASUREMENT CIRCUIT

Figure S1 shows the key elements of the resonator device design: (i) a three turn inductor at the node of the cavity for applying a dc bias across the nanowire; (ii) symmetric coupling capacitors at the input and output of the cavity to measure microwave transmission; and (iii) the final electron beam lithography layer for contacting the nanowire source and drain. A completed device is mounted in a sample holder, as shown in Fig. S2b. To apply wide bandwidth signals to the gate electrode M, a filtered dc line is combined with an attenuated coax line at a bias-tee on the sample holder.

Figure S2a shows the measurement circuit for the experiment. The Colby progammable delay line is used a variable phase shifter to calibrate the Marki IQ mixer. The DL Instruments current preamplifier was run on its battery power supply in order to float its input. The Mini-Circuits ZVA-213 amplifier was placed at the input of the splitter to reduce pulse reflections. In later measurements (Fig. 4e–f), this amplifier was found to cause sample heating and so an additional 20 dB attenuator was placed after the splitter. In Fig. 4e–f, the EDSR drive was also gated during readout to improve the measurement visibility.

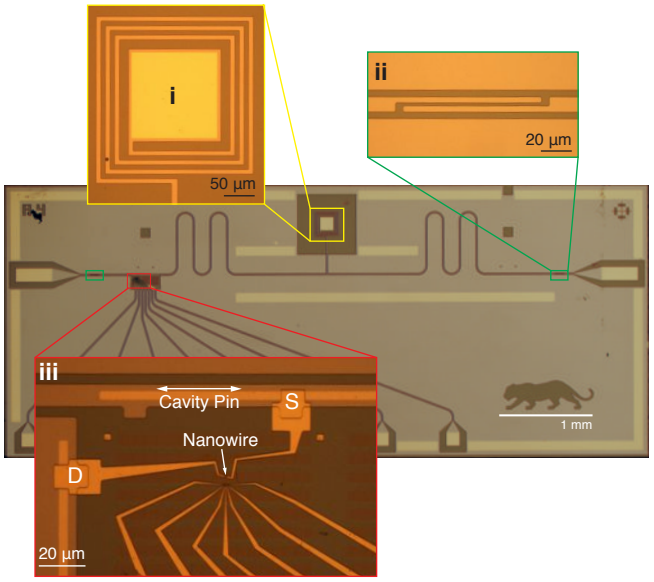

FIG. S1: **Hybrid DQD/superconducting resonator device.** Optical micrograph of a device similar to the one measured. Shown in the expanded views are, **i,** the spiral inductor at the cavity node, **ii,** the input/output coupling capacitors and, **iii,** the nanowire device contact layer.

2. RESONATOR RESPONSE

Figure S3a–b shows the phase and amplitude response of the cavity resonance, as measured using a network analyzer. Prior to sweeping an in-plane magnetic field, the quality factor of the cavity was measured to be $Q \approx 2400$. Following several field sweeps, Figure S3c shows the field dependence of the cavity resonance with the extracted resonance frequency, f_0, and quality factor shown in Fig. S3d–e. After several field sweeps, the quality factor reduced to $Q \approx 2100$ at zero field and $Q \approx 1740$ at 90 mT. There is a substantial shift at $B \approx 11$ mT, most likely due to the Al wirebonds going from superconducting to normal. The input/output coupling capactors were designed to give $Q \sim 10000$ and for a bare resonator with similar coupling capacitors, but without the nanowire device and dc tap spiral inductor, we measured $Q \approx 10890$. Given our estimated 1 MHz spin-cavity coupling strength, we would require $Q > 10000$ at 15 GHz to reach the strong coupling regime. We anticipate that this could be readily achieved by making the following technical improvements: 1) The degradation of Q due to the field could be compensated for by better aligning the field parallel to the Nb film and by working with thinner Nb films and Au wirebonds. 2) Given that the dc tap seems to substantially reduce the Q, next generation samples could have an improved bias tap or no bias tap at all. 3) The high density of gate electrode metal in the qubit notch may also result in additional resonator loss. Future devices could eliminate all unused metal, thereby increasing the Q.

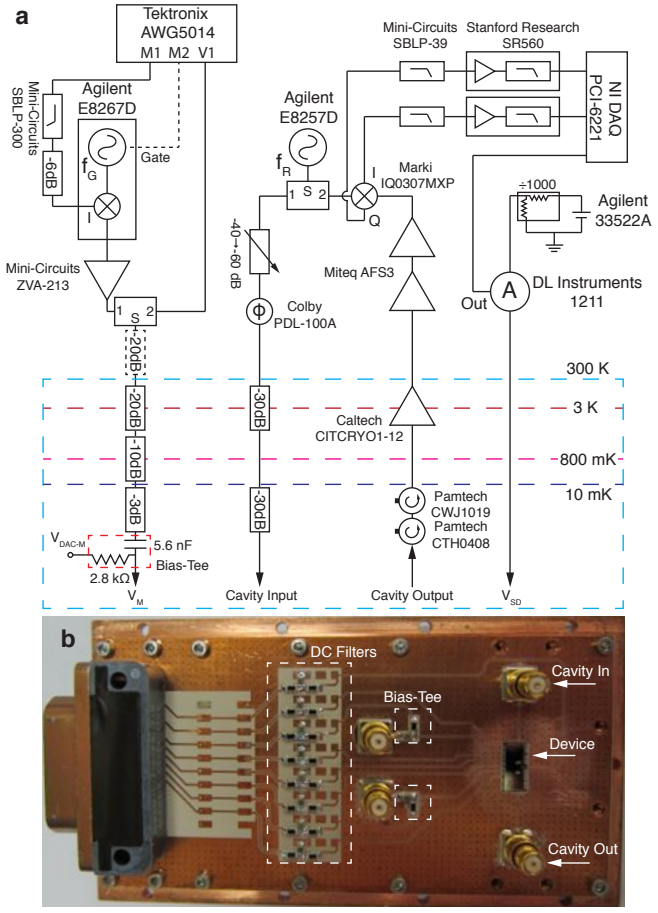

FIG. S2: **Measurement schematic and high frequency sample holder. a,** Schematic of the measurement setup showing the V_M fast gate line used for detuning pulses and EDSR drive and circuits for microwave homodyne detection and current measurement. Omitted are the filtered dc lines for the gate electrodes. **b,** Photograph of the high frequency sample holder.

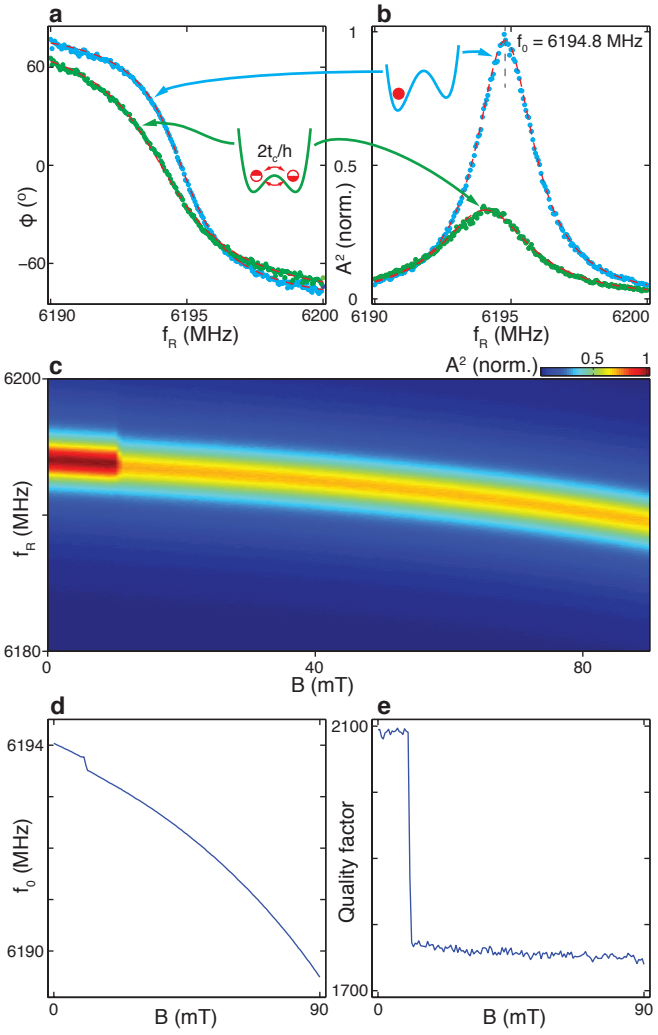

FIG. S3: **Resonator response. a–b,** Phase and normalized amplitude of the microwave field plotted as a function of f_R at the interdot charge transition in Fig. 2b (green curve) and in Coulomb blockade (blue curve). **c,** Normalized amplitude of the microwave field as a function of f_R and magnetic field B in Coulomb blockade. **d–e,** Resonance frequency, f_0, and quality factor as a function of magnetic field, B, as extracted from the data in **c**.

3. CHARGE STABILITY DIAGRAM AND PAULI BLOCKADE

The cavity transmission is sensitive to charge dynamics in the double quantum dot (DQD) and allows for a measurement of the stability diagram. We work in the many electron regime, $N_L \sim N_R \sim 20$, where $N_L(N_R)$ is the number of electrons in the left(right) dot. In dc transport, spin selection rules lead to current rectification at certain charge transitions [26]. For example, in a two-electron double quantum dot, the transition from a $(N_L, N_R) = (1, 1)$ triplet state to a $(0, 2)$ singlet state is blocked due to Pauli exclusion. However, reversing the sign of V_{SD} changes the direction of electron flow and lifts the Pauli blockade since a $(0, 2)$ singlet to $(1, 1)$ singlet state is allowed. Pauli blockade, combined with single charge sensing, allows readout of spin qubits in semiconductor quantum dots [3].

The DQD charge stability diagram is measured in Fig. S4a by probing the phase response of the microwave cavity as a function of the gate voltages V_L and V_R. Figure S4b shows the current measured through the DQD as a function of the gate voltages V_L and V_R for the same

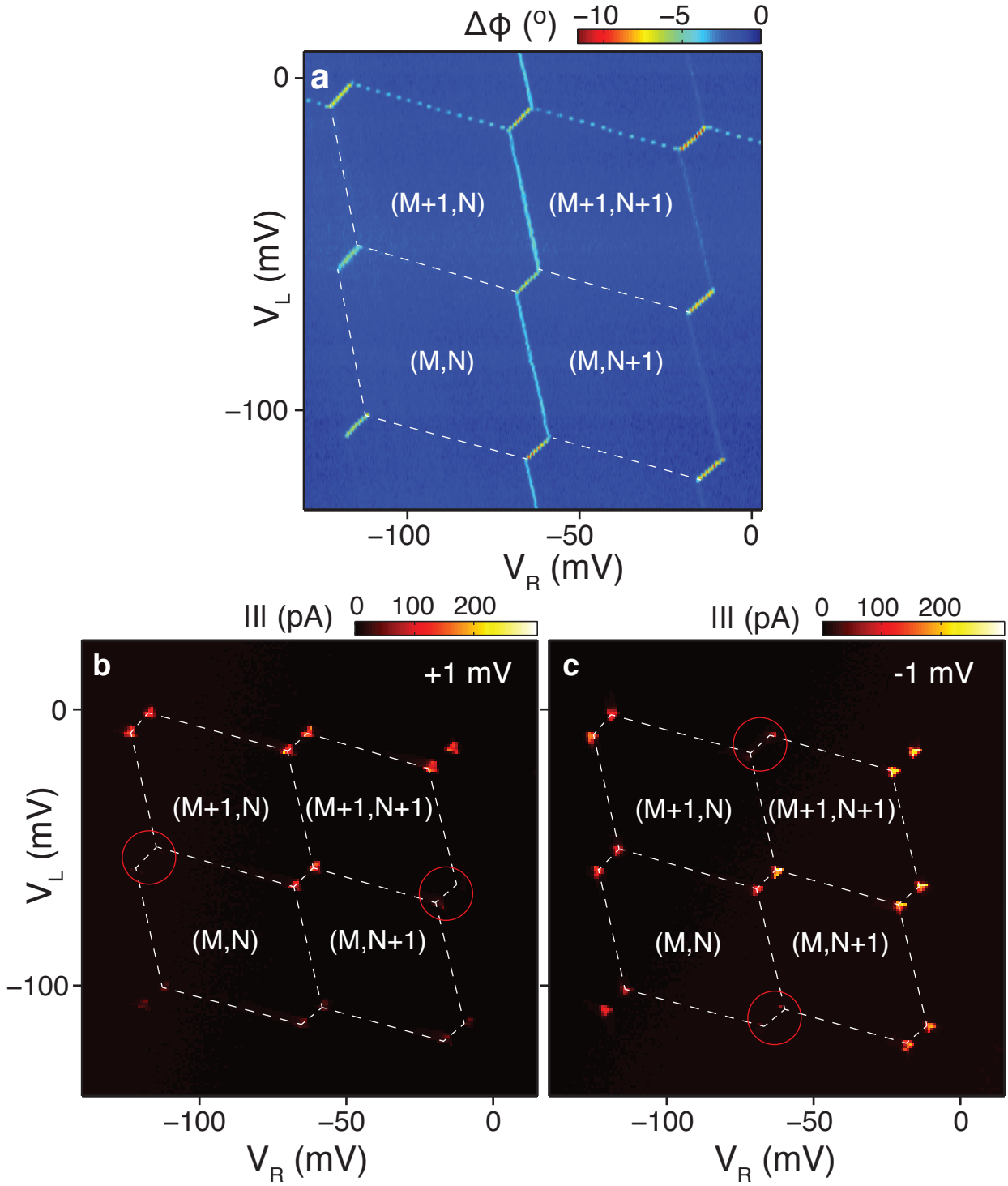

FIG. S4: **Charge stability diagram and Pauli spin blockade. a,** Phase response of the resonator as a function of left and right gate voltages, V_{L} and V_{R}. **b–c,** Current through the nanowire as a function of V_{L} and V_{R} for $V_{\mathrm{SD}} = +1$ mV and $V_{\mathrm{SD}} = -1$ mV. At zero magentic field we observe Pauli spin blockade at the interdot charge transitions circled in red.

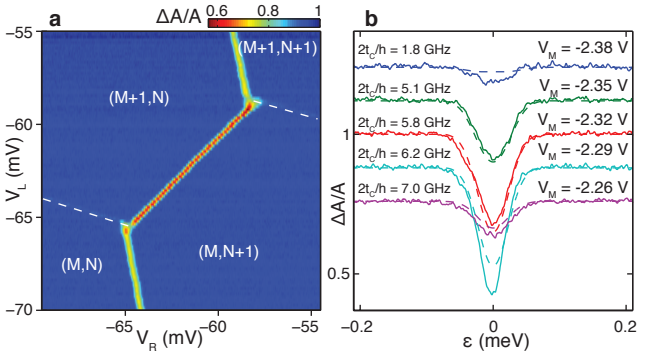

FIG. S5: **Resonator Magnitude Response. a,** Magnitude response of the cavity as a function of gate voltages V_{L} and V_{R} near the $(M{+}1,\, N) \leftrightarrow (M,\, N{+}1)$ charge transition. The corresponding phase response data are shown in Fig. 2a. **b,** Magnitude response measured as a function of DQD detuning, ϵ, for a range of tunnel couplings, t_{C}, as set by V_{M}. The corresponding phase response data are shown in Fig. 2d. Data are offset for clarity.

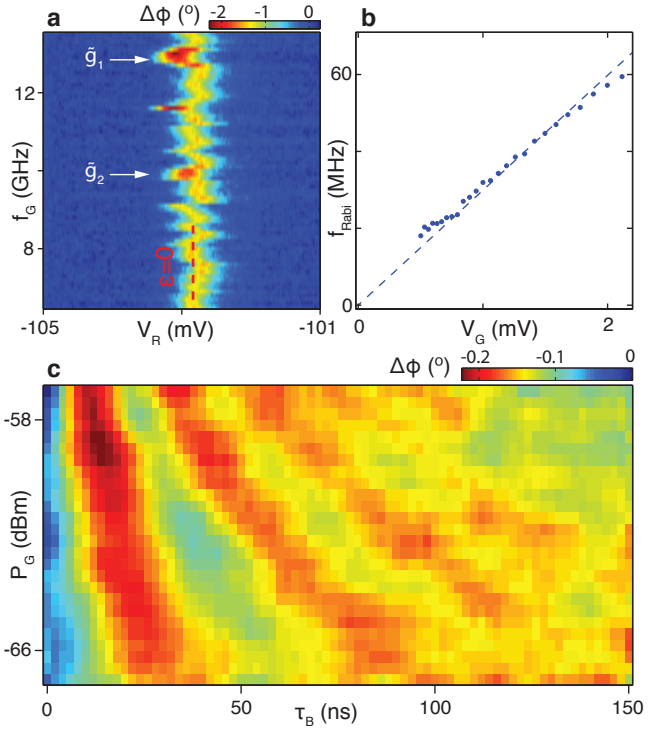

FIG. S6: **EDSR Data extraction. a,** Spectroscopy data used to extract the vertical trace in Fig. 4c for $B = 90$ mT. The arrows indicate the two spin resonance conditions. **b,** Rabi oscillation frequency for the data in Fig. 4e as a function of gate drive, $V_{\mathrm{G}} = 2\sqrt{50\Omega \times P_{\mathrm{G}}}$. **c,** Rabi oscillations for the same sample tuning as in Fig. 4c-d with $B = 90$ mT and $f_{\mathrm{G}} = 13.1$ GHz.

sample tuning. Source-drain bias is fixed at $V_{\mathrm{SD}} = 1$ mV. The application of a finite bias results in finite bias triangles; regions of parameter space where electron tunneling is energetically allowed. Consistent with a simple shell filling model, we observe Pauli blockade at every other charge transition. Upon reversing the sign of bias, $V_{\mathrm{SD}} = -1$ mV, the blockade is lifted, as shown in Fig. S4c. The more widely space gate electrodes in this device prohibit us from reaching the two-electron regime, resulting in slightly smaller excited state and singlet-triplet energies. However, the fundamental process of Pauli blockade, which is a key component of singlet-triplet readout, remains unaffected.

4. RESONATOR MAGNITUDE RESPONSE

In Figs. 2b and 2d we plot the phase response of the cavity. Figures S5a–b show the corresponding magnitude response data. In order to extract the charge-cavity coupling strength, both the phase data (Fig. 2d) and magnitude data (Fig. S5b) were simultaneously fitted to our model.

5. EDSR DATA EXTRACTION

Figure 4b shows the pulse sequence used for coherent spin state control and readout using the microwave cavity. Starting at zero detuning, with a magnetic field applied, intialisation was accomplished through spin relaxation to the $|\Uparrow\Uparrow\rangle$ ground state configuration. The sequence began with a voltage pulse to gate M which would change the detuning to $\epsilon \sim \epsilon' \sim -2$ meV. While at this far detuning position, we would apply an EDSR microwave burst to gate M. The EDSR drive was applied at far detuning in order to minimise inhomogeneous broadening due to charge noise. We then pulsed back to zero detuning for spin readout using the cavity. We measured the time-averaged cavity response over many repetitions ($\sim 10^5$) of the pulse sequence with the cavity drive tone, f_{R}, always on. The measurement time, T_{M}, was set to be comparable to the spin relaxation time, T_1, at zero detuning.

Spin readout using the cavity required a measurement of its response at zero detuning. However, low frequency charge noise meant that, on the timescale of the measurement, the zero detuning position would abruptly shift in gate voltage space, with the magnitude of these shifts comparable to linewidth of the zero detuning peak in the cavity phase response. To extract the data in Figs. 4c–f

we therefore applied a slow (50 Hz) ramp to gate R which swept across zero detuning. For each data point, the detuning ramp was averaged over 100–400 cycles and, after smoothing, the amplitude of the maximum phase shift is extracted. Figure S6a shows the data set from which we extract the vertical trace in Fig. 4c for $B = 90$ mT; a horizontal slice in Fig. S6a gives a single pixel in Fig. 4c. The shifts in the zero detuning position with $V_{\rm R}$ can be readily observed in Fig. S6a.

For lifetime (Fig. 4d) and Rabi oscillations (Fig. 4e–f) measurements, the data are averaged over 10 and 5 separate measurements respectively. Additional smoothing is applied to the data in Fig. 4e–f to improve the visibility of the oscillations. In Fig. 4c we apply a 150 ns detuning pulse and 100 ns microwave burst with a 1 μs period. The data are also levelled along the columns and rows in Fig. 4c. In Fig. 4d we apply a 150 ns detuning pulse and 100 ns microwave burst with a variable period. In Fig. 4e–f we apply a 250 ns pulse with a 2 μs period and variable microwave burst length. A slope of 0.007 deg./ns and the average row value are also subtracted in Fig. 4e–f.

In Fig. 4d the amplitude of the phase shift is normalized to the duty cycle of the pulses by multiplying by $(T_{\rm M} + 150\,{\rm ns})/T_{\rm M}$. The solid curve is then a least squares fit to $\Delta\phi = a_1 + a_2(1 - \exp(-T_{\rm M}/T_1))\frac{T_1}{T_{\rm M}}$. Previous experiments with InAs nanowire spin qubits established $T_1 \gg 1$ μs, however this was measured at far detuning, which may account for the discrepancy with our estimate of $T_1 \sim 1$ μs [8]. Based on experiments using GaAs DQDs we anticipate that the lifetime is strongly detuning dependent and increases away from zero detuning [28].

In Fig. 4f, the fits are to $\Delta\phi = b_1 + b_2\tau_{\rm B} + b_3\cos(\tau_{\rm B}/b_4 + \theta)/\tau_{\rm B}^d$, using the first 80 ns of the data. The decay powers d in Fig. 4f fits I-III are 0.48, 0.45 and 0.40 respectively, consistent with previous experiments [8, 31]. Figure S6b shows the extracted Rabi frequency ($f_{\rm Rabi} = 1/2\pi b_4$) as a function of gate voltage drive. The data show the expected linear dependence.

The data in Fig. 4e–f were acquired following a thermal cycle of the dilution refrigerator and sample retune. Figure S6c shows Rabi oscillations at 13.1 GHz and 90 mT for the same device tuning as in Fig. 4c–d. The improved visibility of the oscillations in Fig. 4e–f followed technical improvements to the experimental setup (Supplementary information, section 1).

6. THEORY

6.1. Cavity transmission and phase shift

We start by considering a double quantum dot with a single electron near the (0,1)–(1,0) charge degeneracy point. An effective Hamiltonian describing this system is the two-level system

$$H_0 = \frac{1}{2}\epsilon\tilde{\sigma}_z + t_{\rm C}\tilde{\sigma}_x \tag{1}$$

where $\tilde{\sigma}_z = |(1,0)\rangle\langle(1,0)| - |(0,1)\rangle\langle(0,1)|$ represents the charge dipole, ϵ is the detuning induced by local gate voltages and also the transmission line resonator, and $t_{\rm C}$ is the coherent tunneling matrix element between the two charge states. To consider the effect of a weak, time-dependent probe field coupling via $\frac{1}{2}\delta\epsilon\cos(\omega_{\rm R}t)\tilde{\sigma}_z$, we diagonalize H_0 into eigenstates with eigenenergies $\Omega_\pm = \pm\frac{1}{2}\Omega = \pm\frac{1}{2}\sqrt{(2t_{\rm C})^2 + \epsilon^2}$. Then, in this basis of eigenstates with $\sigma_z = |\Omega_+\rangle\langle\Omega_+| - |\Omega_-\rangle\langle\Omega_-|$, we obtain the dipole coupling

$$H_{\rm D} = \frac{\delta\epsilon}{2}\cos(\omega_{\rm R}t) \times \left(\frac{\epsilon}{\Omega}\sigma_z + \frac{2t_{\rm C}}{\Omega}\sigma_x\right) \tag{2}$$

Moving to a rotating frame with the unitary

$$U = \exp\left[-\frac{i}{2}(\omega t + \frac{\epsilon\delta\epsilon\sin(\omega_{\rm R}t)}{\hbar\omega_{\rm R}\Omega})\sigma_z\right], \tag{3}$$

and defining

$$\Delta = \frac{\Omega}{\hbar} - \omega_{\rm R} \tag{4}$$

and making a rotating wave approximation for $\omega = \omega_{\rm R}$, we find, to order $\delta\epsilon$,

$$H_{\rm RF,RWA} \approx \frac{\hbar\Delta}{2}\sigma_z + \frac{\delta\epsilon}{4}\frac{2t_{\rm C}}{\Omega}\sigma_x. \tag{5}$$

From our effective Hamiltonian (Eqn. 5) and relaxation through phonons at rate $\sim \gamma$ between the two energy eigenstates of H_0, we can determine the response of the cavity to the quantum dot via linear response theory. Specifically, we need to evaluate the steady state value of the quantum dot density matrix $\rho_{\rm ss}$, and from that determine the field-dependent dipole induced, $d = {\rm Tr}[e\vec{r}\rho_{\rm ss}]$, leading to a Δ-dependent susceptibility $\chi \propto d/\delta\epsilon$ for small detunings Δ.

We now replace the probe term $\frac{1}{4}\delta\epsilon\cos(\omega_{\rm R}t)$ with the voltage from the cavity photons in the rotating frame, taking the form $g_{\rm C}(ae^{-i\omega_{\rm R}t} + a^\dagger e^{i\omega_{\rm R}t})$, where $g_{\rm C}$ is the

vacuum Rabi coupling. In the rotating frame and rotating wave approximation, we obtain an effective description of the cavity and double dot:

$$H_{\rm tot} = \hbar\Delta_0 a^\dagger a + \frac{\hbar\Delta}{2}\sigma_z + \hbar g_{\rm eff}(a\sigma_+ + a^\dagger\sigma_-) \quad (6)$$

$$g_{\rm eff} = g_{\rm C}\frac{2t_{\rm C}}{\Omega} \quad (7)$$

where $\Delta_0 = \omega_0 - \omega_{\rm R}$ is the cavity detuning from the probe field.

To determine the effect this combined double-dot cavity system has on an input probe of the cavity, we use the input operator formalism and develop the Heisenberg-Langevin equations of motion. For simplicity, we assume that the quantum dot stays near its lower energy state with high probability, leading to the replacement $\sigma_z \to -1$. In what follows, $\kappa = \kappa_1 + \kappa_2 + \kappa_i$ is the total cavity decay, where κ_1 and κ_2 are the decay rates through the input and output ports, and κ_i is the internal decay. We then find

$$\dot{a} = -i\Delta_0 a - \frac{\kappa}{2}a + \sqrt{\kappa_1}a_{\rm in,1} + \sqrt{\kappa_2}a_{\rm in,2} - ig_{\rm eff}\sigma_- \quad (8)$$

$$\dot{\sigma}_- = -i\Delta\sigma_- - \frac{\gamma}{2}\sigma_- + \sqrt{\gamma}\mathcal{F} - ig_{\rm eff}a \quad (9)$$

where we will neglect the quantum noise terms $a_{\rm in,2}$ and $\mathcal{F}$, and keep only the classical input field $a_{\rm in,1} \to \alpha$, which is oscillating at frequency $\omega_{\rm R}$. The output of the cavity is then $a_{\rm out,2} = \sqrt{\kappa_2}a - a_{\rm in,2}$. Looking at the steady state and neglecting quantum noise, we find

$$\frac{a_{\rm out,2}}{\alpha} = \frac{-i\sqrt{\kappa_1\kappa_2}}{\Delta_0 - i\kappa/2 + g_{\rm eff}\chi} \quad (10)$$

where the susceptibility of the double quantum dot is $\chi = \frac{g_{\rm eff}}{-\Delta + i\gamma/2}$. The cavity transmission and phase shift are determined by Eqn. 10, with $T = |\frac{a_{\rm out,2}}{\alpha}|^2$ and the phase shift given by $\Delta\phi = -\arg(\frac{a_{\rm out,2}}{\alpha})$.

In fitting the data we assume a qubit lifetime of 15 ns. To account for inhomogenous broadening in the detuning sweeps (Fig. 2d and Fig. S5b) due to low frequency charge noise we convolve the phase and amplitude response of the cavity transmission with a Gaussian of linewidth, σ_ϵ, [32].

6.2. Hamiltonian for the spin qubit

For the case of two electrons in the double dot, with the basis states $|S(0,2)\rangle$, $|S(1,1)\rangle = (|\Uparrow\Downarrow\rangle - |\Downarrow\Uparrow\rangle)/\sqrt{2}$, $|T_+(1,1)\rangle = |\Uparrow\Uparrow\rangle$, $|T_0(1,1)\rangle = (|\Uparrow\Downarrow\rangle + |\Downarrow\Uparrow\rangle)/\sqrt{2}$ and $|T_-(1,1)\rangle = |\Downarrow\Downarrow\rangle$ we have the following Hamiltonian,

$$H_2 = \begin{bmatrix} -\frac{1}{2}\epsilon & t_{\rm C} & 0 & 0 & 0 \\ t_{\rm C} & \frac{1}{2}\epsilon & 0 & \frac{1}{2}(\tilde{g_1}-\tilde{g_2})\mu_{\rm B}B & 0 \\ 0 & 0 & \frac{1}{2}\epsilon - \frac{1}{2}(\tilde{g_1}+\tilde{g_2})\mu_{\rm B}B & 0 & 0 \\ 0 & \frac{1}{2}(\tilde{g_1}-\tilde{g_2})\mu_{\rm B}B & 0 & \frac{1}{2}\epsilon & 0 \\ 0 & 0 & 0 & 0 & \frac{1}{2}\epsilon + \frac{1}{2}(\tilde{g_1}+\tilde{g_2})\mu_{\rm B}B \end{bmatrix}, \quad (11)$$

where $\tilde{g_1}$ and $\tilde{g_2}$ are the g-factors of the two dots and we have assumed relatively weak spin orbit in comparison to $t_{\rm C}$. For the data in Fig. 3 and 4C–D, $\tilde{g_1} \approx 10.5$, $\tilde{g_2} \approx 8$ and from the detuning dependence of the phase and magnitude response at $B = 0$, we estimate $2t_{\rm C}/h \sim 6$ GHz. At large negative detuning, the eigenstates are $|S(0,2)\rangle$, $|\Uparrow\Downarrow\rangle$, $|\Downarrow\Uparrow\rangle$, $|T_+(1,1)\rangle$ and $|T_-(1,1)\rangle$ due the large difference in g-factors for the two dots.

6.3. Dispersive spin measurement

We can consider the response of the cavity-double dot system for the singlet and triplet manifolds by realizing that the susceptibility for the singlet states qualitatively follows that of the single charge, while the triplet states are in the far detuned limit near the charge transition due to the large single dot singlet-triplet energy splitting (~ 1.7 meV). Thus we can look at the phase shift or transmission of a probe field and, in a regime where $g_{\rm eff}\chi$ is appreciable for the singlet states (and negligible for the triplet states), observe a difference in these quantities for the singlet when compared to the triplet. This allows a dispersive readout of singlet states, in analogy to spin-to-charge conversion and low-frequency sensing as employed in prior experiments. In the case of our experiment where the g-factors of the two dots are significantly different, the T_0-like state will relax rapidly to

the lower singlet-like state, enabling dispersive readout of both spin transitions.

* Electronic address: petta@princeton.edu

[3] Hanson, R., Kouwenhoven, L. P., Petta, J. R., Tarucha, S. & Vandersypen, L. M. K. Spins in few-electron quantum dots. *Rev. Mod. Phys.* **79**, 1217-1265 (2007).

[8] Nadj-Perge, S., Frolov, S. M., Bakkers, E. & Kouwenhoven, L. P. Spin-orbit qubit in a semiconductor nanowire. *Nature* **468**, 1084-1087 (2010).

[26] Ono, K., Austing, D. G., Tokura, Y. & Tarucha, S. Current Rectification by Pauli exclusion in a weakly coupled double quantum dot system. *Science* **297**, 1313-1317 (2002).

[28] Johnson, A. C. *et al.* Triplet-singlet spin relaxation via nuclei in a double quantum dot. *Nature* **435**, 925-928 (2005).

[31] Koppens, F. H. L. *et al.* Universal phase shift and non-exponential decay of driven single-spin oscillations. *Phys. Rev. Lett.* **99**, 106803 (2007).

[32] Petersson, K. D., Petta, J. R., Lu, H. & Gossard, A. C. Quantum coherence in a one-electron semiconductor charge qubit. *Phys. Rev. Lett.* **105**, 246804 (2010).